Published by Avanti Publishers

Journal of Advanced Thermal Science Research

ISSN (online): 2409-5826

Convective Heat Transfer Performance of Hybrid Nanofluid in a Wavy-walled Thermal System with Localized Heating

Anirban Chattopadhyay[1,*], Krishno D. Goswami[2] and Sayantan Roy[1]

[1]*Education Directorate, Higher Education Department Bikash Bhavan, Kolkata 700091, India*
[2]*Department of Mathematics, SRM Institute of Science and Technology Kattankulathur, Tamilnadu 603 203, India*

ARTICLE INFO

Article Type: Research Article

Academic Editor: Xueqiang Shi

Keywords:
MHD
Hybrid nanofluid
Compact scheme
Localized heating
Wavy-walled cavity

Timeline:
Received: October 03, 2025
Accepted: November 28, 2025
Published: December 29, 2025

Citation: Chattopadhyay A, Goswami KD, Roy S. Convective heat transfer performance of hybrid nanofluid in a wavy-walled thermal system with localized heating. J Adv Therm Sci Res. 2025; 12: 150-169.

DOI: https://doi.org/10.15377/2409-5826.2025.12.9

ABSTRACT

This work ahead deals with the impact of magnetic field dependent viscosity (MFDV) on natural convection heat transfer of Ag - MgO (50%-50%) water hybrid nanoliquid. The considered thermal system is a wavy-walled cavity with heat source placed at bottom wall. The governing equations (Navier-Stokes equations) constituting streamfunction (ψ)- vorticity (ζ) formulation with energy equation are solved by adopting a compact finite difference fourth order scheme. Meanwhile, the flow domain which is influenced by several factors including Hartmann number ($10 \leq Ha \leq 50$), hybrid nanoparticles volume fraction ($0 \leq \varphi_{hnp} \leq 0.02$), Rayleigh number ($10^4 \leq Ra \leq 10^6$), orientation angle of magnetic field ($0^0 \leq \gamma \leq 90^0$), magnetic number ($0 \leq \delta_0 \leq 1$), different configurations (Configuration-I and Configuration-II) and internal heat generation or absorption ($-5 \leq Q \leq 5$) is analyzed generously. Experimentally based correlations for thermal conductivity and dynamic viscosity have been used throughout the study. The objective of this study is to design a thermal system with better thermal performance. The results are analyzed through streamlines and isotherms contour plots and average Nusselt numbers. The fluid flow and heat transfer are significantly influenced by buoyancy force, heat generation/absorption coefficient The outcomes show that the geometric parameters can be used as an excellent controller of the thermal performance inside the wavy chamber.

*Corresponding Author
Email: animath81@rediffmail.com
Tel: +(91) 9732082380

1. Introduction

The enhancement of convective heat transfer in thermal systems represents a pivotal research area due to its extensive applications across various scientific and industrial domains [1-6]. In particular, natural convection within complex geometries presents significant challenges and opportunities for performance improvement. Over recent decades, the utilization of advanced working fluids has emerged as a prominent strategy for augmenting thermal transport capabilities [7-12]. Among these, nanofluids−engineered suspensions of nanoscale particles (1—100 nm) in conventional base fluids—have demonstrated remarkable potential for heat transfer enhancement [13, 14], attracting considerable research interest into their behavior in diverse configurations.

Beyond the fluid medium itself, the geometry of the enclosure is a critical factor influencing convective performance. In this context, wavy-walled cavities have attracted considerable attention due to their ability to modify flow patterns and thermal fields, thereby influencing heat transfer rates [15-17]. The corrugations of such walls can disrupt boundary layer development and enhance fluid mixing, which is highly relevant for applications like solar collectors [18, 19], electronic cooling systems [20], and automotive radiators [21]. The interplay between the complex geometry and the fluid dynamics underscores the need for a deeper understanding of these systems.

Parallel to advancements in geometry, the evolution of the working fluids has progressed significantly. While unitary nanofluids containing a single type of nanoparticle have shown promising results [22, 23], recent focus has shifted toward hybrid nanofluids. These fluids, which combine multiple nanomaterials, leverage synergistic effects to achieve superior thermal characteristics and improved heat transfer performance compared to their mono-variant counterparts [24, 25]. Comprehensive reviews by researchers including Sarkar *et al*. [26] and Tyagi *et al*. [27] have extensively documented the potential of these hybrid systems in pushing the boundaries of thermal management.

To further control and optimize thermal performance within such systems, the strategic placement of heat sources and the application of external fields have been explored. The presence of localized heating, for instance, introduces another layer of complexity; studies by Mohebbi *et al*. [28] and Chamkha *et al*. [29] have demonstrated that heater positioning is a decisive factor for thermal performance. Complementing this, external magnetic fields offer a powerful tool for actively modulating transport phenomena [30, 31]. Research into magnetohydrodynamic (MHD) effects on nanofluids [32, 33] has revealed that Lorentz forces can effectively suppress or guide convection currents, providing a means to control heat transfer rates. Additional phenomena such as thermal radiation [34] and the presence of porous media [35] further enrich this complex interplay, creating a multi-faceted problem.

Despite these extensive investigations, a synergistic analysis combining wavy boundaries, hybrid nanofluids, and strategic localized heating remains relatively unexplored. Previous studies have often focused on these aspects in isolation, leaving a gap in understanding their combined effect on thermal performance. Therefore, the present work aims to address this gap by numerically investigating the convective heat transfer performance of a hybrid nanofluid within a wavy-walled enclosure subjected to localized heating. This study systematically examines various heater configurations to identify optimal arrangements for maximizing heat transfer enhancement. The findings are expected to provide valuable insights for the design of more efficient and compact thermal systems in advanced engineering applications.

2. Mathematical Modeling Procedure

This section presents the tri-hybrid nanofluid correlations that are taken into consideration as well as the mathematical formulation of the topic under consideration. Different subsections additionally include the governing equations, boundary conditions, and quantitative thermal activity measurement for the current situation.

2.1. Problem Statement

The problem under consideration is described in the two-dimensional (2D) physical domain in Fig. (**1**). Furthermore, Fig. (**1**) displays a perspective of the grid that is used to discretize the computing domain. A distorted

cavity in nature with a characteristic length L is represented by the geometry with wavy walls. The following transformation functions have been used to convert the physical domain into a computation square domain in order to address the current distorted cavity:

$$X = \xi[1 - A(1 - cos(d\pi\eta) - A(1 - cos(d\pi\eta)] + A(1 - cos(d\pi\eta)) \quad (1)$$

$$Y = \eta \quad (2)$$

$$\xi = \frac{X - A + Acos(d\pi Y)}{1 - 2A + 2Acos(d\pi Y)} \quad (3)$$

$$\eta = Y \quad (4)$$

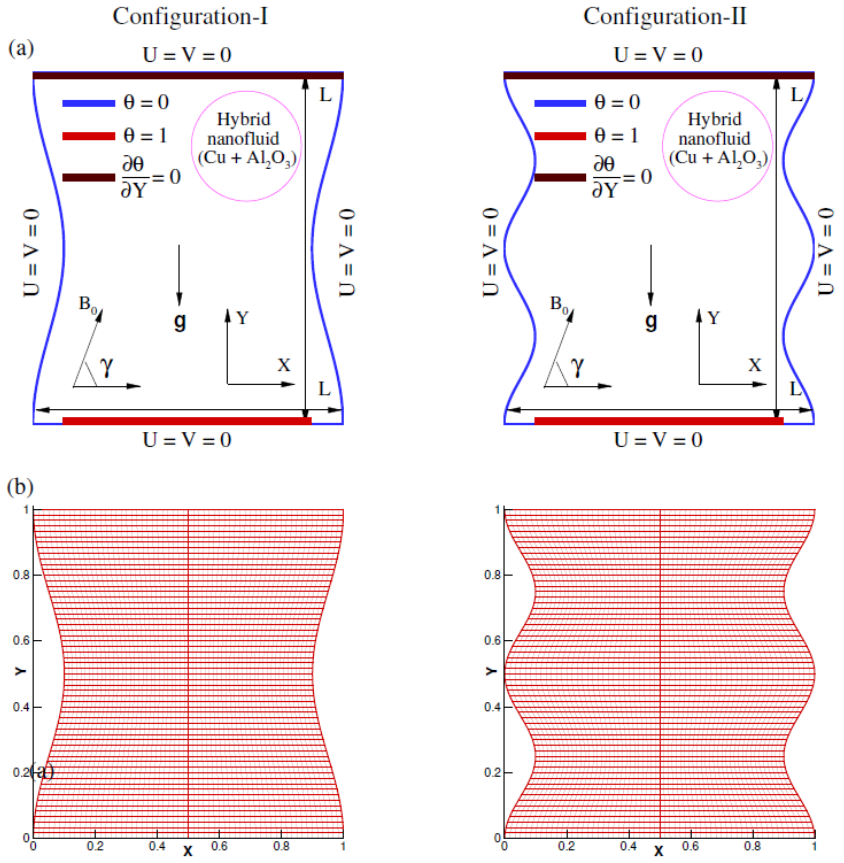

Figure 1: (**a**) Schematic diagram of the physical model and (**b**) the grid distribution considered for the physical domain. Two configurations (Configuration-I and Configuration-II) have been considered depending on the undulation of the vertical walls. All four boundaries are at rest, the vertical walls are kept at cold temperature compare to the heater placed at bottom boundary. Top wall is adiabatic.

Where, the parameters that govern the geometric characteristics, including the wavy contraction ratio and the vertical walls undulation, are $A = 0.05$, and d. $d = 2$ forms single undulation and to construct double undulation we condider $d = 4$. The domain of interest is filled with Ag-MgO $(50\% - 50\%)$ water hybrid nanoliquid. In addition, two different configurations (Configuration-I - Configuration-II) have been considered depending on the number of wall undulation of the system. A localized uniform heat source of length $\frac{4L}{6}$ is placed on bottom wall. The applied thermal boundary conditions on the vertical walls form temperature gradient within the cavity which is orthogonal to the direction of gravity. On the other hand the temperature gradient is along the direction of gravity for the heater placed on the bottom wall. Consequently, the arrangement of different undulation and the subsequent configuration are being portrayed in Fig. (**1**). The heater is maintained at a constant temperature T_h, higher than the temperature T_c ($T_c < T_h$) on the cold sinusoidal walls. Moreover, the non heating locations of the bottom wall is

maintained in cold temperature T_c. The flow convection is a natural type and is induced by the temperature gradient between the heated walls and the cold deformed walls. All four boundaries are kept in rest by assuming conditions that the velocity components (u, v) are to be zero. An external uniform magnetic field vector $\boldsymbol{B} = (B_x, B_y)$ with fixed amplitude B0 is affected in the cavity. The imposed magnetic field makes an orientation γ with the axis x such that $\gamma = cot^{-1}\left(\frac{B_x}{B_y}\right)$. The present analysis is based on the unsteady, single-phase, Newtonian, laminar, incompressible hybrid nanofluid model with constant thermo-physical properties.

2.2. Governing Equations in Usual Form

The flow physics is modeled mathematically through the following governing equations [36];

Continuity:

$$\partial_x u + \partial_y v = 0, \tag{5}$$

x momentum:

$$\left(u\partial_x u + v\partial_y u\right) = -\frac{1}{\rho_{hnf}}\partial_x p + \frac{\eta_{hnf}}{\rho_{hnf}}[\partial_{xx}u + \partial_{yy}u] \tag{6}$$

$$+\frac{\sigma_{hnf}}{\rho_{hnf}}B_0^2(vsin\gamma cos\gamma - usin^2\gamma),$$

y momentum:

$$\left(u\partial_x v + v\partial_y v\right) = -\frac{1}{\rho_{hnf}}\partial_y p + \frac{\eta_{hnf}}{\rho_{hnf}}[\partial_{xx}v + \partial_{yy}v] \tag{7}$$

$$+\frac{1}{\rho_{hnf}}g\beta_{hnf}(T - T_c) + \frac{\sigma_{hnf}}{\rho_{hnf}}B_0^2(usin\gamma cos\gamma - vcos^2\gamma),$$

Energy:

$$u\partial_x T + v\partial_y T = \alpha_{hnf}[\partial_{xx}T + \partial_{yy}T] + \frac{Q_0}{(\rho C_p)_{hnf}}(T - T_c) \tag{8}$$

In the momentum equations (6-7), $\eta_{tnf} = \mu_{tnf}(1 + \vec{\delta}\cdot\vec{B})$. The variation coefficient of viscosity $\vec{\delta}$ has been taken to be isotropic, $\delta_x = \delta_y = \delta^*$. A uniform magnetic field B_0 acts along the inclined direction γ with respect to horizontal axis.

2.3. Mathematical Formulation through Non-dimensional Form

These Eqs. (5)-(8) are transformed into non-dimensional view by applying the following parameters [36] $P = \frac{pL^2}{\rho_f\alpha_f^2}$, $X = \frac{x}{L}$, $Y = \frac{y}{L}$, $U = \frac{uL}{\alpha_f}$, $V = \frac{vL}{\alpha_f}$, $\theta = \frac{T-T_c}{T_h-T_c}$, $Q = \frac{Q_0L^2}{k_f}$, $Ec = \frac{\alpha_f^2}{L^2(c_p)_f(T_h-T_c)}$, $Pr = \frac{\nu_f}{\alpha_f}$, $Ra = \frac{g\beta_f L^3\Delta T}{\alpha_f\nu_f}$, $Ha = B_0L\sqrt{\frac{\sigma_f}{\mu_f}}$, $\delta_0 = B_0\delta^*$

and are formulated as follows [36]:

$$\frac{\partial U}{\partial X} + \frac{\partial V}{\partial Y} = 0, \tag{9}$$

$$U\frac{\partial U}{\partial X} + V\frac{\partial U}{\partial Y} = -\frac{\rho_f}{\rho_{hnf}}\frac{\partial P}{\partial X} + \frac{\nu_{hnf}}{\nu_f}Pr[1 + \delta_0(cos\gamma + sin\gamma)]\nabla^2 U + \tag{10}$$

$$\frac{\sigma_{hnf}}{\sigma_f}\frac{\rho_f}{\rho_{hnf}}Ha^2Pr(Vsin(\gamma)cos(\gamma) - Usin^2(\gamma)),$$

$$U\frac{\partial V}{\partial X} + V\frac{\partial V}{\partial Y} = -\frac{\rho_f}{\rho_{hnf}}\frac{\partial P}{\partial Y} + \frac{\nu_{hnf}}{\nu_f}Pr[1 + \delta_0(cos\gamma + sin\gamma)]\nabla^2 V \tag{11}$$

$$+\frac{\rho_f}{\rho_{hnf}}\frac{(\rho\beta)_{hnf}}{(\rho\beta)_f}RaPr\theta+\frac{\sigma_{hnf}}{\sigma_f}\frac{\rho_f}{\rho_{hnf}}Ha^2Pr(U)sin(\gamma)cos(\gamma)-Vcos^2(\gamma)).$$

$$U\frac{\partial\theta}{\partial X}+V\frac{\partial\theta}{\partial Y}=\frac{k_{hnf}}{k_f}\frac{(\rho c_p)_f}{(\rho c_p)_{hnf}}\nabla^2\theta+Q\frac{(\rho c_p)_f}{(\rho c_p)_{hnf}}\theta \tag{12}$$

2.4. Streamfunction-Vorticity-Energy Equations in $X-Y$ Plane

Streamfunction [36]:

$$\nabla^2\psi=-\zeta, \tag{13}$$

Vorticity:

$$-\frac{\nu_{hnf}}{\nu_f}Pr[1+\delta_0(cos\gamma+sin\gamma)]\nabla^2\zeta+U\frac{\partial\zeta}{\partial X}+V\frac{\partial\zeta}{\partial Y}= \tag{14}$$

$$\frac{(\rho\beta)_{hnf}}{(\rho\beta)_f}\frac{\rho_f}{\rho_{hnf}}RaPr\frac{\partial\theta}{\partial X}+\frac{\sigma_{hnf}\rho_f}{\rho_{hnf}\sigma_f}Ha^2Pr$$

$$\times\left(sin(\gamma)cos(\gamma)\left(\frac{\partial U}{\partial X}-\frac{\partial V}{\partial Y}\right)+sin^2(\gamma)\frac{\partial U}{\partial Y}-cos^2(\gamma)\frac{\partial V}{\partial X}\right),$$

Energy:

$$U\frac{\partial\theta}{\partial X}+V\frac{\partial\theta}{\partial Y}=\frac{k_{hnf}}{k_f}\frac{(\rho c_p)_f}{(\rho c_p)_{hnf}}\nabla^2\theta+Q\frac{(\rho c_p)_f}{(\rho c_p)_{hnf}}\theta. \tag{15}$$

2.5. Streamlines-Vorticity-Energy Equations in $\xi-\eta$ Plane

Streamfunction :

$$\begin{aligned}\frac{X_\eta^2+Y_\eta^2}{J^2}\frac{\partial^2\psi}{\partial\xi^2}\quad&-2\frac{X_\eta X_\xi+Y_\eta Y_\xi}{J^2}\frac{\partial^2\psi}{\partial\xi\,\partial\eta}+\frac{X_\xi^2+Y_\xi^2}{J^2}\frac{\partial^2\psi}{\partial\eta^2}+\left[\frac{Y_\eta Y_{\xi\eta}-Y_\xi Y_{\eta\eta}+X_\eta X_{\xi\eta}-X_\xi X_{\eta\eta}}{J^2}\right.\\&\left.-\frac{(Y_\eta^2+X_\eta^2)J_\xi-J_\eta(Y_\xi Y_\eta+X_\xi X_\eta)}{J^3}\right]\frac{\partial\psi}{\partial\xi}+\left[\frac{Y_\xi Y_{\xi\eta}-Y_\eta Y_{\xi\xi}+X_\xi X_{\xi\eta}-X_\eta X_{\xi\xi}}{J^2}\right.\\&\left.-\frac{J_\xi(Y_\eta Y_\xi+X_\eta X_\xi)-(X_\xi^2+Y_\xi^2)J_\eta}{J^3}\right]\frac{\partial\psi}{\partial\eta}=-\zeta\end{aligned} \tag{16}$$

Vorticity:

$$\begin{aligned}&-\frac{\nu_{\mathrm{hnf}}}{\nu_{\mathrm{f}}}Pr[1+\delta_0(\cos\gamma+\sin\gamma)]\left[\frac{X_\eta^2+Y_\eta^2}{J^2}\frac{\partial^2\zeta}{\partial\xi^2}-2\frac{X_\eta X_\xi+Y_\eta Y_\xi}{J^2}\frac{\partial^2\zeta}{\partial\xi\partial\eta}\right.\\&\quad+\frac{X_\xi^2+Y_\xi^2}{J^2}\frac{\partial^2\zeta}{\partial\eta^2}+\left(\frac{Y_\eta Y_{\xi\eta}-Y_\xi Y_{\eta\eta}+X_\eta X_{\xi\eta}-X_\xi X_{\eta\eta}}{J^2}\right.\\&\quad\left.-\frac{(Y_\eta^2+X_\eta^2)J_\xi-J_\eta(Y_\xi Y_\eta+X_\xi X_\eta)}{J^3}\right)\frac{\partial\zeta}{\partial\xi}+\left(\frac{Y_\xi Y_{\xi\eta}-Y_\eta Y_{\xi\xi}+X_\xi X_{\xi\eta}-X_\eta X_{\xi\xi}}{J^2}\right.\\&\quad\left.\left.-\frac{J_\xi(Y_\eta Y_\xi+X_\eta X_\xi)-(X_\xi^2+Y_\xi^2)J_\eta}{J^3}\right)\frac{\partial\zeta}{\partial\eta}\right]+U\frac{1}{J}\left(Y_\eta\frac{\partial\zeta}{\partial\xi}-Y_\xi\frac{\partial\zeta}{\partial\eta}\right)\\&\quad+V\frac{1}{J}\left(X_\xi\frac{\partial\zeta}{\partial\eta}-X_\eta\frac{\partial\zeta}{\partial\xi}\right)=\frac{(\rho\beta)_{\mathrm{hnf}}}{(\rho\beta)_{\mathrm{f}}}\frac{\rho_{\mathrm{f}}}{\rho_{\mathrm{hnf}}}RaPr\frac{1}{J}\left(Y_\eta\frac{\partial\theta}{\partial\xi}-Y_\xi\frac{\partial\theta}{\partial\eta}\right)\\&\quad+\frac{\sigma_{\mathrm{hnf}}\rho_{\mathrm{f}}}{\rho_{\mathrm{hnf}}\sigma_{\mathrm{f}}}Ha^2Pr\left\{\sin\gamma\cos\gamma\frac{1}{J}\left(Y_\eta\frac{\partial U}{\partial\xi}-Y_\xi\frac{\partial U}{\partial\eta}\right)-\frac{1}{J}\left(X_\xi\frac{\partial V}{\partial\eta}-X_\eta\frac{\partial V}{\partial\xi}\right)\right.\\&\qquad\left.+\sin^2\gamma\frac{1}{J}\left(X_\xi\frac{\partial U}{\partial\eta}-X_\eta\frac{\partial U}{\partial\xi}\right)-\cos^2\gamma\frac{1}{J}\left(Y_\eta\frac{\partial V}{\partial\xi}-Y_\xi\frac{\partial V}{\partial\eta}\right)\right\}\end{aligned} \tag{17}$$

Energy:

$$
\begin{aligned}
&U\frac{1}{J}\left(Y_\eta\frac{\partial\theta}{\partial\xi}-Y_\xi\frac{\partial\theta}{\partial\eta}\right)+V\frac{1}{J}\left(X_\xi\frac{\partial\theta}{\partial\eta}-X_\eta\frac{\partial\theta}{\partial\xi}\right)\\
&=\frac{k_{\text{hnf}}}{k_f}\frac{(\rho c_p)_f}{(\rho c_p)_{\text{hnf}}}\Big[\frac{X_\eta^2+Y_\eta^2}{J^2}\frac{\partial^2\theta}{\partial\xi^2}-2\frac{X_\eta X_\xi+Y_\eta Y_\xi}{J^2}\frac{\partial^2\theta}{\partial\xi\,\partial\eta}+\frac{X_\xi^2+Y_\xi^2}{J^2}\frac{\partial^2\theta}{\partial\eta^2}\\
&+\left(\frac{Y_\eta Y_{\xi\eta}-Y_\xi Y_{\eta\eta}+X_\eta X_{\xi\eta}-X_\xi X_{\eta\eta}}{J^2}-\frac{(Y_\eta^2+X_\eta^2)J_\xi-J_\eta(Y_\xi Y_\eta+X_\xi X_\eta)}{J^3}\right)\frac{\partial\theta}{\partial\xi}\\
&+\left(\frac{Y_\xi Y_{\xi\eta}-Y_\eta Y_{\xi\xi}+X_\xi X_{\xi\eta}-X_\eta X_{\xi\xi}}{J^2}-\frac{J_\xi(Y_\eta Y_\xi+X_\eta X_\xi)-(X_\xi^2+Y_\xi^2)J_\eta}{J^3}\right)\frac{\partial\theta}{\partial\eta}\Big]\\
&+Q\frac{(\rho c_p)_f}{(\rho c_p)_{\text{hnf}}}\theta.
\end{aligned}
\tag{18}
$$

2.6. Boundary Specifications

The imposed boundary conditions strongly influence the convective flow and heat transfer behavior. For better clarity, the dimensional and corresponding non-dimensional boundary conditions are presented in a parallel tabular form in Table **1**.

2.6.1. Dimensional and Non-dimensional Boundary Conditions

Table 1: Dimensional and non-dimensional boundary conditions.

Boundary	Dimensional Form	Non-dimensional Form
Left wall ($x=0$)	$u=v=0,\ T=T_c$	$U=V=0,\ \theta=0$
Right wall ($x=L$)	$u=v=0,\ T=T_c$	$U=V=0,\ \theta=0$
Top wall ($y=L$)	$u=v=0,\ \frac{\partial T}{\partial y}=0$	$U=V=0,\ \frac{\partial\theta}{\partial Y}=0$
Bottom wall ($y=0$)	$u=v=0,$	$U=V=0,$
	$T=T_h$ for $\frac{L}{6}\le x\le\frac{5L}{6}$,	$\theta=1$ for $\frac{1}{6}\le X\le\frac{5}{6}$,
	$T=T_c$ for $0\le x\le\frac{L}{6}\ \cup\ \frac{5L}{6}\le x\le L$	$\theta=0$ for $0\le X\le\frac{1}{6}\ \cup\ \frac{5}{6}\le X\le 1$

2.6.2. Streamfunction–vorticity Boundary Conditions

The boundary conditions for streamfunction (ψ) and vorticity (ζ) in the computational (ξ,η) plane are written as

$$
\begin{aligned}
&\psi=0, && 0\le\xi\le 1,\ 0\le\eta\le 1,\\
&\zeta=-\frac{\partial^2\psi}{\partial\eta^2}, && \text{at } \eta=0 \text{ and } \eta=1,\\
&\zeta=-\frac{\partial^2\psi}{\partial\xi^2}, && \text{at } \xi=0 \text{ and } \xi=1.
\end{aligned}
\tag{19}
$$

The no-slip condition at all solid walls is enforced by prescribing $\psi=0$, while the corresponding wall vorticity is obtained from the second derivatives of the streamfunction. Since the present study employs a higher-order compact (HOC) finite difference scheme, special care is taken in evaluating these derivatives near the boundaries. In this context, the readers are referred to the works of [40, 41] for detailed formulations of the higher-order compact (HOC) scheme and its boundary implementations.

2.7. Chemo-physical Properties of Nanoliquids and Hybrid Nanoliquids

The effective characteristics of nanoliquid and hybrid nanofluid are associated with the host liquid (water) and Ag-MgO solid hybrid particles. Ag-MgO nanoparticle pair is a combination of a noble metal and a ceramic oxide. Silver (Ag) has very high thermal conductivity, on the other hand Magnesium oxide (MgO) adds thermal stability and dispersion support. Various chemico-physical properties of water and hybrid nanofluid are portrayed in Table **2**. Theoretical correlations for the formulation of the nanofluid and hybrid nanoliquid properties [37, 38] are

portrayed in Table **3**. On the other hand, Table **4** summarizes the experimental based correlations of heat conductivity and viscosity for the hybrid-nanoliquid [39]. The variations of thermo-physical properties are assumed to be negligible with respect the temperature. The composed liquid is electrically conductive subject to the assumptions of no chemical reaction, negligible thermal radiation, no slippage between water molecule and composite particles and low viscus dissipation effects. There is a negligible effect of induced magnetic field due to the motion of electrically conducting hybrid nanofluid compared to the imposed external magnetic field.

Table 2: Physicochemical characteristics of host liquid, Ag and MgO nano-size particles [46, 47].

Property	Host Liquid (Water)	Ag	MgO
ρ (Kg·m−3)	977.1	10,490	3560
μ (Pa·s)	8.55×10^{-4}	-	-
c_p (J·Kg−1 ·K−1)	4179	235	955
k (W·m−1 ·K−1)	0.613	429	45
α (m2 ·s−1)	1.47×10^{-7}	-	-
$\beta \times 10^{-5}$ (K−1)	21	1.89	1.05
σ (Ωm)−1	0.05	6.30×10^{7}	1.42×10^{-3}
$Pr\left(=\frac{\mu_f}{\rho\alpha}\right)$	5.95	-	-

Table 3: Theoretical correlations for the formulation of hybrid nanofluids properties [37, 38].

Nanofluid Properties	Hybrid Nanofluids Model
Density	$\rho_{hnf} = (1-\varphi_{hnp})\rho_f + \varphi_{Ag}\rho_{Ag} + \varphi_{MgO}\rho_{MgO}$
Heat capacitance	$(\rho c_p)_{hnf} = (1-\varphi_{hnp})(\rho c_p)_f + \varphi_{Ag}(\rho c_p)_{Ag} + \varphi_{MgO}(\rho c_p)_{MgO}$
Thermal diffusivity	$(\alpha_{hnf}) = \frac{k_{hnf}}{(\rho C_p)_{hnf}}$
Buoyancy coefficient	$(\rho\beta)_{hnf} = (1-\varphi_{hnp})(\rho\beta)_f + \varphi_{Ag}(\rho\beta)_{Ag} + \varphi_{MgO}(\rho\beta)_{MgO}$
Electrical conductivity	$\frac{\sigma_{hnf}}{\sigma_f} = 1 + \frac{3\left(\frac{\varphi_{Ag}\sigma_{Ag}+\varphi_{MgO}\sigma_{MgO}}{\sigma_f} - \varphi_{hnp}\right)}{\left(\frac{\varphi_{Ag}\sigma_{Ag}+\varphi_{MgO}\sigma_{MgO}}{\sigma_f\varphi_{hnp}} + 2\right) - \left(\frac{\varphi_{Ag}\sigma_{Ag}+\varphi_{MgO}\sigma_{MgO}}{\sigma_f} - \varphi_{hnp}\right)}$
Effective Thermal conductivity	$\frac{k_{hnf}}{k_f} = \frac{\frac{\varphi_{Ag}k_{Ag}+\varphi_{MgO}k_{MgO}}{\varphi_{hnp}} + 2k_f + 2(\varphi_{Ag}k_{Ag} + \varphi_{MgO}k_{MgO}) - 2\varphi k_f}{\frac{\varphi_{Ag}k_{Ag}+\varphi_{MgO}k_{MgO}}{\varphi_{hnp}} + 2k_f - (\varphi_{Ag}k_{Ag} + \varphi_{MgO}k_{MgO}) + \varphi k_f}$
Effective viscosity	$\frac{\mu_{hnf}}{\mu_f} = (1-\varphi_{hnp})^{-2.5}, \quad where \quad \varphi_{hnp} = \varphi_{Ag} + \varphi_{MgO}$

Table 4: Experimental based correlations for effective thermal conductivity and effective viscosity hybrid nanofluids [39].

Nanofluid Properties	Hybrid Nanofluids Model
Effective Thermal conductivity	$\frac{k_{hnf}}{k_f} = \left(\frac{0.1747\times 10^5 + \varphi_{hnp}}{0.1747\times 10^5 - 0.1498\times 10^6\varphi_{hnp} + 0.1117\times 10^7\varphi_{hnp}^2 + 0.1997\times 10^8\varphi_{hnp}^3}\right)$
	$0 \le \varphi_{hnp} \le 3.0$
Effective viscosity	$\frac{\mu_{nf}}{\mu_f} = 1 + 32.795\varphi_{hnp} - 7214\varphi_{hnp}^2 + 714600\varphi_{hnp}^3 - 0.1941\times 10^8\varphi_{hnp}^4$
	$0 \le \varphi_{hnp} \le 2.0$

2.8. Heat Transfer Activity

The thermal performance, which is a key concern for convective flows that must be observed in care to improve the efficiency of any thermal system. In transport dynamics, it is measure by a nondimensional parameter called Nusselt number. In this work, the average Nusselt number evaluated for localized heating in bottom boundary (Nu)is given by:

$$Nu = \frac{\int \ Nu_{loc} dX}{\int \ dX}. \tag{20}$$

The corresponding expression of Eqn. (20) in $\xi - \eta$ plane takes the form as:

$$Nu = \frac{\int \ Nu_{loc} d\xi}{\int \ d\xi}. \tag{21}$$

3. Numerical Procedure

This section presents the description of the methodology which has been applied for the present simulation and the corresponding validations. At the beginning of this numerical simulation, we have transformed the non-dimensional governing Eqns. (16 - 18), from the physical X -Y plane to the computational ξ -η plane by using the functions given in Eqns. (1) and (2). The expression of the essential operators to carry out the transformation from physical plane to computational plane are as follows:

$$\frac{\partial}{\partial x} = \frac{1}{J}\left[\left(\frac{\partial}{\partial \xi}\right)\left(\frac{\partial y}{\partial \eta}\right) - \left(\frac{\partial}{\partial \eta}\right)\left(\frac{\partial y}{\partial \xi}\right)\right], \tag{22}$$

$$\frac{\partial}{\partial y} = \frac{1}{J}\left[\left(\frac{\partial}{\partial \eta}\right)\left(\frac{\partial x}{\partial \xi}\right) - \left(\frac{\partial}{\partial \xi}\right)\left(\frac{\partial x}{\partial \eta}\right)\right], \tag{23}$$

$$\begin{aligned}\frac{\partial^2}{\partial x^2} = \frac{1}{|J|^2}\Big[& \left(\frac{\partial y}{\partial \eta}\right)^2 \frac{\partial^2}{\partial \xi^2} - 2\frac{\partial y}{\partial \eta}\frac{\partial y}{\partial \xi}\frac{\partial^2}{\partial \xi\,\partial \eta} + \left(\frac{\partial y}{\partial \xi}\right)^2 \frac{\partial^2}{\partial \eta^2} \\ & + \frac{\partial y}{\partial \eta}\frac{\partial^2 y}{\partial \xi\,\partial \eta}\frac{\partial}{\partial \xi} - \frac{\partial y}{\partial \xi}\frac{\partial^2 y}{\partial \eta^2}\frac{\partial}{\partial \xi} + \frac{\partial y}{\partial \xi}\frac{\partial^2 y}{\partial \xi\,\partial \eta}\frac{\partial}{\partial \eta} - \frac{\partial y}{\partial \eta}\frac{\partial^2 y}{\partial \xi^2}\frac{\partial}{\partial \eta}\Big] \\ -\frac{1}{|J|^3}\Big[& \left(\frac{\partial y}{\partial \eta}\right)^2 \frac{\partial |J|}{\partial \xi}\frac{\partial}{\partial \xi} - \frac{\partial y}{\partial \xi}\frac{\partial y}{\partial \eta}\frac{\partial |J|}{\partial \eta}\frac{\partial}{\partial \xi} + \left(\frac{\partial y}{\partial \xi}\right)^2 \frac{\partial |J|}{\partial \eta}\frac{\partial}{\partial \eta}\Big],\end{aligned} \tag{24}$$

$$\begin{aligned}\frac{\partial^2}{\partial y^2} = \frac{1}{|J|^2}\Big[& \left(\frac{\partial x}{\partial \eta}\right)^2 \frac{\partial^2}{\partial \xi^2} - 2\frac{\partial x}{\partial \eta}\frac{\partial x}{\partial \xi}\frac{\partial^2}{\partial \xi\,\partial \eta} + \left(\frac{\partial x}{\partial \xi}\right)^2 \frac{\partial^2}{\partial \eta^2} \\ & + \frac{\partial x}{\partial \eta}\frac{\partial^2 x}{\partial \xi\,\partial \eta}\frac{\partial}{\partial \xi} - \frac{\partial x}{\partial \xi}\frac{\partial^2 x}{\partial \eta^2}\frac{\partial}{\partial \xi} + \frac{\partial x}{\partial \xi}\frac{\partial^2 x}{\partial \xi\,\partial \eta}\frac{\partial}{\partial \eta} - \frac{\partial x}{\partial \eta}\frac{\partial^2 x}{\partial \xi^2}\frac{\partial}{\partial \eta}\Big] \\ -\frac{1}{|J|^3}\Big[& \left(\frac{\partial x}{\partial \eta}\right)^2 \frac{\partial |J|}{\partial \xi}\frac{\partial}{\partial \xi} - \frac{\partial x}{\partial \xi}\frac{\partial x}{\partial \eta}\frac{\partial |J|}{\partial \eta}\frac{\partial}{\partial \xi} + \left(\frac{\partial x}{\partial \xi}\right)^2 \frac{\partial |J|}{\partial \eta}\frac{\partial}{\partial \eta}\Big],\end{aligned} \tag{25}$$

$$\begin{aligned}\frac{\partial^2}{\partial x\,\partial y} = \frac{1}{|J|^2}\Big[& \frac{\partial y}{\partial \eta}\frac{\partial x}{\partial \eta}\frac{\partial^2}{\partial \xi^2} - \left(\frac{\partial y}{\partial \eta}\frac{\partial x}{\partial \xi} + \frac{\partial y}{\partial \xi}\frac{\partial x}{\partial \eta}\right)\frac{\partial^2}{\partial \xi\,\partial \eta} + \frac{\partial y}{\partial \xi}\frac{\partial x}{\partial \xi}\frac{\partial^2}{\partial \eta^2} \\ & + \frac{1}{2}\left(\frac{\partial y}{\partial \eta}\frac{\partial^2 x}{\partial \xi^2} - \frac{\partial y}{\partial \xi}\frac{\partial^2 x}{\partial \eta^2} + \frac{\partial x}{\partial \eta}\frac{\partial^2 y}{\partial \xi^2} - \frac{\partial x}{\partial \xi}\frac{\partial^2 y}{\partial \eta^2}\right)\frac{\partial}{\partial \xi} \\ & + \frac{1}{2}\left(\frac{\partial y}{\partial \xi}\frac{\partial^2 x}{\partial \xi\,\partial \eta} - \frac{\partial y}{\partial \eta}\frac{\partial^2 x}{\partial \xi\,\partial \eta} + \frac{\partial x}{\partial \xi}\frac{\partial^2 y}{\partial \xi\,\partial \eta} - \frac{\partial x}{\partial \eta}\frac{\partial^2 y}{\partial \xi\,\partial \eta}\right)\frac{\partial}{\partial \eta}\Big],\end{aligned} \tag{26}$$

where, $J = X_\xi Y_\eta - X_\eta Y_\xi$ is the Jacobian of the coordinate transformation. Using these operators the Eqns. (22 - 26) can be expressed as:

$$a\frac{\partial^2 \widehat{\Phi}}{\partial \xi^2} + g\frac{\partial^2 \widehat{\Phi}}{\partial \xi \partial \eta} + b\frac{\partial^2 \widehat{\Phi}}{\partial \eta^2} + c\frac{\partial \widehat{\Phi}}{\partial \xi} + d\frac{\partial \widehat{\Phi}}{\partial \eta} + p\widehat{\Phi} = f, \tag{27}$$

where the coefficients a, g, b, c, d and p are the transformed form of the corresponding coefficients in physical plane and f is the transformed part of the source function in the computational plane. It is mentioned here that $\Phi_{i,j}$ (Φ stands for ψ, ζ and θ) denotes the approximate value of the function $\hat{\phi}$ at a mesh point (ξ_i, η_j). In this

context, the readers are referred to the works of [40, 41] for detail formulations of the higher order compact (HOC) scheme.

Using Taylors series approximation

$$(\varphi_{\xi})_{i,j} = \left(\delta_{\xi}\varphi_{i,j} - \frac{h^2}{6}\delta_{\xi}^2\varphi_{\xi_{i,j}}\right) + O(h^4). \tag{28}$$

$$(\varphi_{\eta})_{i,j} = \left(\delta_{\eta}\varphi_{i,j} - \frac{h^2}{6}\delta_{\eta}^2\varphi_{\eta_{i,j}}\right) + O(h^4). \tag{29}$$

Furthermore, the nonlinearity of the governing equations as well as the curvilinear domain leads us to make use of BiCGStab [42] method to solve the obtained discretized system of algebraic equations. The convergence criterion for the steady state solution is specified as:

$$max\,|\,\chi_{i,j}^{(\gamma+1)} - \chi_{i,j}^{(\gamma)}| < 0.5 \times 10^{-6}, \tag{30}$$

where, $\chi_{i,j}^{(\gamma+1)}$ and $\chi_{i,j}^{(\gamma)}$ indicate numerical values of $\psi_{i,j}$, $\zeta_{i,j}$ or $\theta_{i,j}$ at consecutive outer iterations. The entire strategy can be accomplished in the algorithm given as follows:

1. n -th iteration step:
2. Initialize $\psi, \zeta, \theta, U, V, \psi_X, \psi_Y, \zeta_X, \zeta_Y, \theta_X, \theta_Y, U_X, U_Y, V_X$ and V_Y.
3. $(n+1)$ -th iteration step:
4. Solve Eqs. (28) and (29) for $\theta_X, \theta_Y, \zeta_X, \zeta_Y, \psi_X, \psi_Y, U_X, U_Y, V_X$ and V_Y using 1(a).

The entire computation has been carried out using an in-house code which has been written in our lab using C programming language. Typically the CPU computation time required in PC with Intel(R) Core(TM) i3-2100 CPU @ 3.10GHz processor and 4 GB RAM is around 20 to 25 minutes.

3.1. Mesh Study

In the current study, a uniform orthogonal mesh is used. The mesh independence analysis has been implemented for Configuration-I under critical conditions: $Ha = 30$, $Q = 2$, $\gamma = \frac{\pi}{2}$, $\delta_0 = 1$ and $\varphi_{hnp} = 2\%$. Table **5** demonstrates the grid sensitivity analysis for various grid sizes versus Nusselt number (Nu) and streamfunction $|\psi|_{Max}$. Among the grid sizes 31×31, 61×61 and 121×121 for the grid 61×61 the changes in the Nu and $|\psi|_{Max}$ values are in the tolerance level ($\leq 5\%$) and it is applied for all cases.

Table 5: Errors associated with the average Nusselt number (Nu) and streamfunction $|\psi|_{max}$ on the grids at $Ha = 30$, $\varphi_{hnp} = 0.02$, $\delta_0 = 1$, $Q = 2$, $\gamma = \frac{\pi}{2}$ in Configuration-I.

Ra	Grids	Nu	$\Delta = \frac{\lvert Nu_{i\times j} - Nu_{61\times 61}\rvert}{Nu_{61\times 61}} \times 100\%$	$\lvert\psi\rvert_{max}$	$\Delta = \frac{\lvert\lvert\psi\rvert_{max_{i\times j}} - \lvert\psi\rvert_{max_{61\times 61}}\rvert}{\lvert\psi\rvert_{max_{61\times 61}}} \times 100\%$
	31×31	5.859	4.86%	0.298	2.71%
$Ra = 10^4$	61×61	5.158	0%	0.306	0%
	121×121	6.458	4.87%	0.313	2.15%
	31×31	7.857	4.66%	5.054	2.81%
$Ra = 10^5$	61×61	8.241	0%	5.200	0%
	121×121	8.637	4.80%	5.309	2.1%
	31×31	13.533	4.75%	13.803	2.85%
$Ra = 10^6$	61×61	14.208	0%	22.279	0%
	121×121	14.896	4.85%	14.471	1.85%

3.2. Verification

The validation of the numerical solution is an important part to validate the in-house code for a simulation with other published work. In order to ensure the authentication of our applied solver in present study, several comparisons have been carried in tabulated form (Table **6**) as well as graphical form (Fig. **2**). Table **6** presents a comprehensive validation for Nu_{av} among experimental data [43], various numerical techniques [44] and present study. The purpose of this validation is to establish the used higher order compact scheme with the existing literature. In this validation, we have considered three different volume fractions of Al_2O_3 – H_2O nanoliquid. The obtained results demonstrate excellent agreement, further affirming the accuracy of the computational model. Fig. (**2**) depicts another validation between Al-Amiri *et al*. [45] and our computed results for the streamlines and isotherm patterns. The type of the flow is a mixed convection within a wavy walled cavity. In this validation, the non-dimensional parameters are considered as $Pr = 0.71$, $Ri = 0.01$, $Gr = 10^4$, $\lambda = 3$ and $A = 0.05$. A good match is observed between present work with [45]. All these validations give us confidence that our in-house code can accurately compute the solution and thereby this code is used to study the problem considered here.

Table 6: Comparison of Nu_{av} between the experimental results, various numerical techniques and the present work for various φ, Ra_{nf} and Pr_{nf}.

Nu av	$\varphi = 1\%$	$\varphi = 2\%$	$\varphi = 3\%$	Average Variation From
	$Ra_{nf} = 7.74547 \times 10^7$	$Ra_{nf} = 6.675118 \times 10^7$	$Ra_{nf} = 5.6020687 \times 10^7$	$existing\ resilts$
	$Pr_{nf} = 7.0659$	$Pr_{nf} = 7.3593$	$Pr_{nf} = 7.8353$	
Exp [43]	32.2037	31.0905	29.0769	1.2%
$FEM - 2D$ [44]	31.8633	31.6085	28.2160	0.97%
$FEM - 3D$ [44]	32.7829	32.1833	31.3692	3%
$FDM - 2D$ [44]	30.6570	30.5030	30.2050	2.2%
$LBM - 2D$ [44]	30.0010	29.8370	29.6180	4.4%
$Obtained\ data$	32.0521	31.2089	30.1379	-

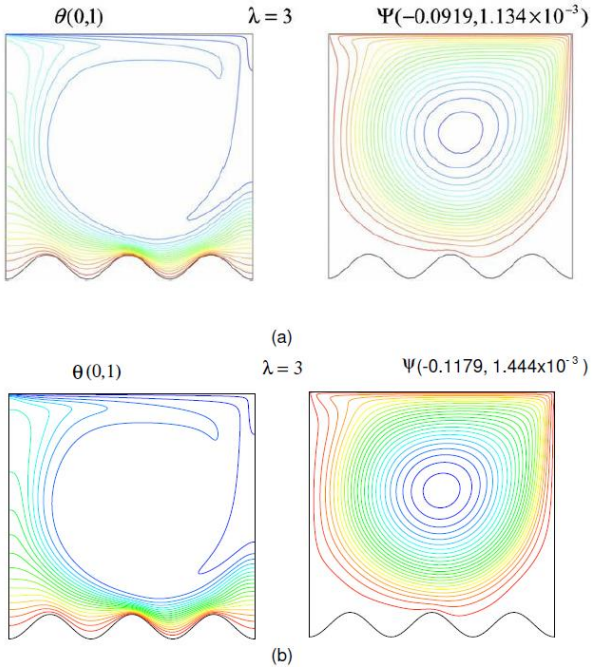

Figure 2: Comparison of the streamline and temperature contours between (**a**) numerical work [45] and (**b**) present study.

4. Results & Discussion

This section presents the results and their physical interpretation for a system analyzed over a broad parametric space. The study explores the effects of buoyancy ($10^4 \leq Ra \leq 10^6$), magnetic field ($10 \leq Ha \leq 50$). Further considerations include internal heat generation ($-5 \leq Q \leq 5$), magnetic field inclination ($0 \leq \gamma \leq \pi/2$), and nanoparticles volume fraction ($0 \leq \varphi_{hnp} \leq 0.02$). The analysis is conducted with fixed values for the magnetic number ($\delta_0 = 1$) and Prandtl number ($Pr = 5.95$). The practical relevance for the considered parameters with such ranges include, MHD cooling systems with moderate magnetic fields, electronic cooling / thermal management of small devices, hybrid nanofluid stability, and chemical reactors; internal heat sources. Two different geometrical configurations have been considered depending on the single and double vertical wavy walls.

4.1. Visualization of Transport Phenomena through Contour Plots

The 2-D visualization of streamlines and isotherms through contour plots are the effective ways to analyze the transport phenomena within the flow domain. The streamfunction values (ψ) indicates the volumetric flow rate in every region of the flow domain. Whereas, the isotherms indicates the distribution of thermal energy within the domain. It is very important to consider the role of various non-dimensional physical parameters and their impacts on streamlines and isotherms.

4.1.1. Effect of Thermal Buoyancy for Different Configuration of the Considered Domain

The influence of thermal buoyancy, governed by the Rayleigh number (Ra), on the flow structure and heat transfer is depicted in Fig. (**3**) and Fig. (**4**). These figures illustrate the evolution of the transport field, visualized via streamlines and isotherms, for the single undulation (Configuration-I) and double undulation (Configuration-II) geometries, respectively. The results are presented for a range of Ra, with all other parameters held constant at $Ha = 30$, $Q = 2$, $\delta_0 = 1$, $\gamma = \pi/2$, and $\varphi_{\mathrm{hnp}} = 2\%$.

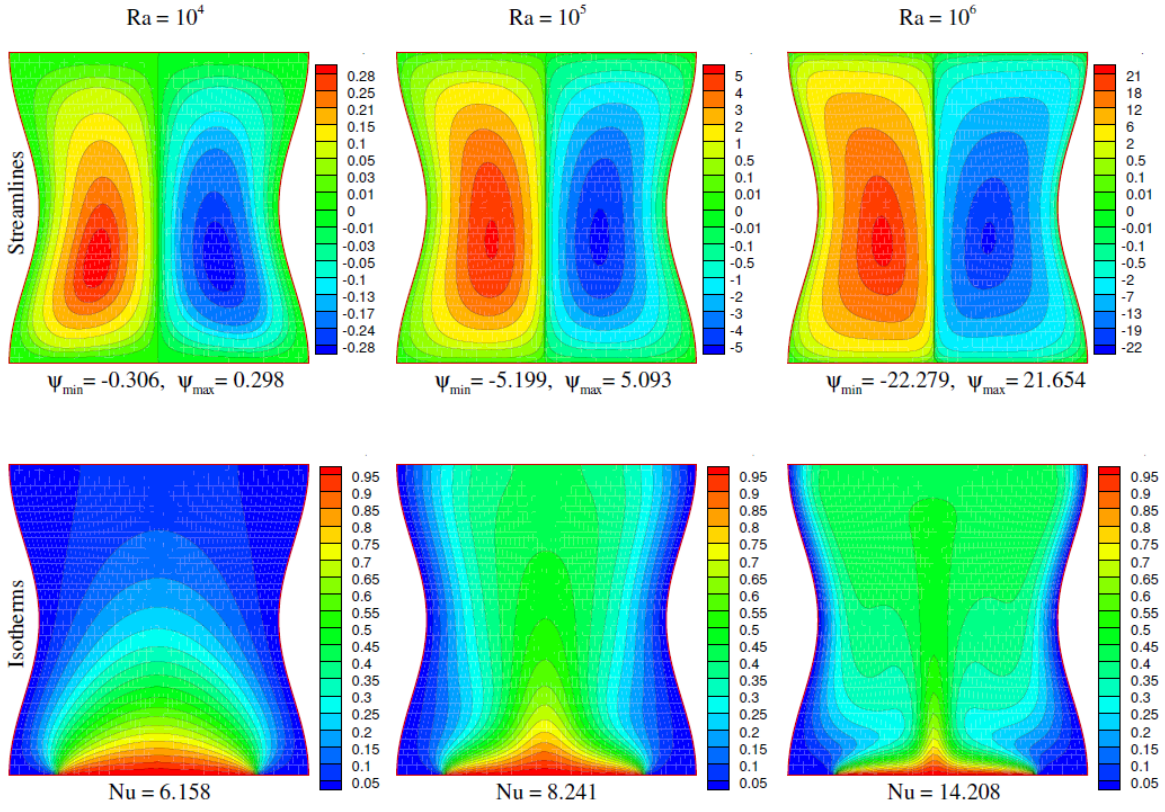

Figure 3: Streamlines and isotherms profiles for single undulation configuration when $Ha = 30$, $Q = 2$, $\delta_0 = 1$, $\gamma = \frac{\pi}{2}$ and $\varphi_{hnp} = 2\%$ due to various Ra.

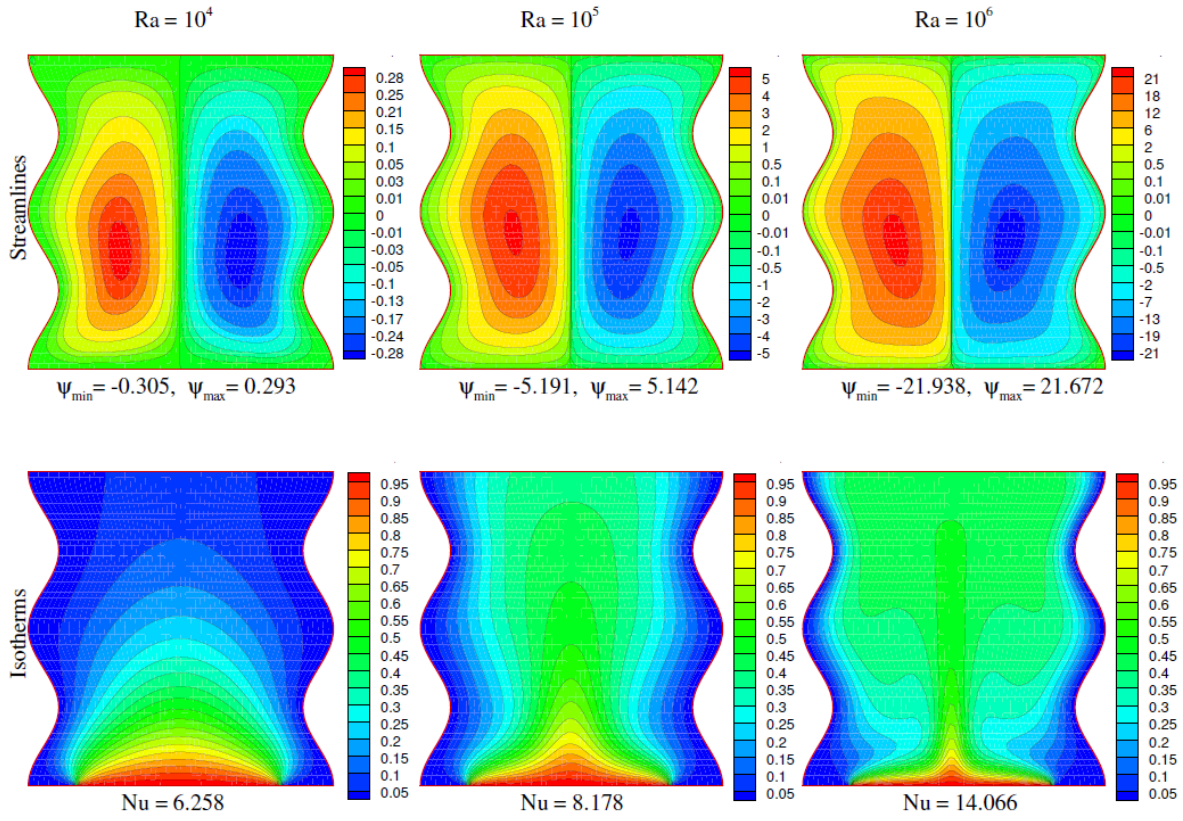

Figure 4: Streamlines and isotherms profiles for double undulation configuration when $Ha = 30$, $Q = 2$, $\delta_0 = 1$, $\gamma = \frac{\pi}{2}$ and $\varphi_{hnp} = 2\%$ due to various Ra.

For the single undulation geometry (Fig. **3**), the flow and thermal fields exhibit a classical response to increasing Ra. At low Ra, the flow is weak and dominated by two symmetrical large recirculating vortex that fills the primary cavity. The corresponding isotherms are nearly parallel and vertical, characteristic of a conduction-dominated regime where heat transfer is primarily due to diffusion, and the damping effect of the magnetic field ($Ha = 30$) is significant. As Ra increases, the intensifying buoyancy force strengthens the primary vortices and begins to distort the flow, drawing it towards the undulation. The isotherms become increasingly curved, indicating the onset of convective heat transfer, with the development of thermal plumes from the heated surfaces. At the highest Ra, two strong, asymmetric primary vortex is established, and the isotherms are highly distorted, showing thin thermal boundary layers and significant mixing in the core, signifying a transition to a convection-dominated regime.

In stark contrast, the double undulation geometry (Fig. **4**) fosters a far more complex flow structure. At low Ra, the flow is not a single large cell but is already structured into multiple, weaker vortices nestled within the cavities created by the undulations. The isotherms, while still relatively linear, show a more complex distribution due to the intricate geometry. As Ra increases, this multi-cellular structure is not suppressed but instead intensified and becomes the defining feature of the flow. Secondary vortices strengthen and become more distinct, creating a compartmentalized flow field. The isotherms evolve into a highly complex and wavy pattern, tightly packed within the undulations, indicating localized regions of intense heat transfer. At high Ra, the flow is characterized by vigorous, interacting recirculation zones in each cavity, and the isotherms reveal strong, localized thermal plumes, demonstrating that heat transfer is enhanced and governed by the complex geometry guiding the buoyancy-driven flow.

4.1.2. Role of Internal Heat Effects for Different Configuration of the Considered Domain

The interplay between buoyancy-driven flow and internal heat effects on the system's thermal performance is described in Fig. (**5**) (for one undulation) and Fig. (**6**) (for two undulations) through the streamlines and isotherms

contours. The results are presented for various Q, with all other parameters held constant at $Ha = 30$, $Ra = 10^6$, $\delta_0 = 1$, $\varphi_{\text{hnp}} = 0.02$, and $\gamma = \pi/2$, a configuration indicative of a strong, buoyancy-driven flow regime.

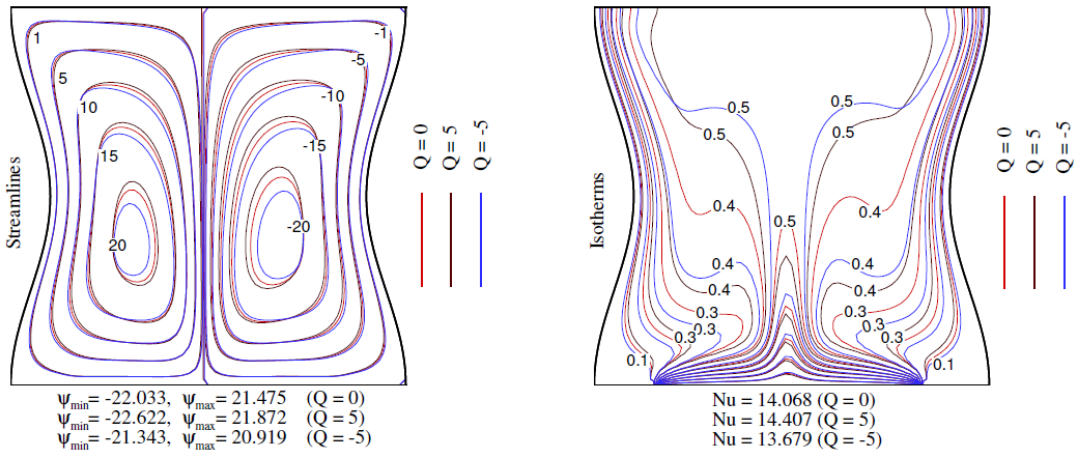

Figure 5: Streamlines (left) and isotherm contours (right) for the single-undulation wall configuration illustrating the effect of the heat generation/absorption parameter Q ($Q = 0{,}5, -5$) on the flow structure and thermal field at $Ha = 30$, $Ra = 10^6$, $\delta_0 = 1$, $\gamma = \pi/2$, and $\varphi_{hnp} = 2\%$. Increasing Q intensifies thermal gradients and strengthens circulation, whereas negative Q weakens convection and thickens the thermal boundary layers.

Fig. (**5**) reveals the significant impact of the internal heat source/sink parameter Q on the convective dynamics within the single undulation enclosure. At a high Rayleigh number ($Ra = 10^6$), the flow is inherently vigorous, but the direction and intensity of this flow are critically modulated by Q.

For $Q > 0$, representing an internal heat source, the fluid within the entire domain experiences an additional heating effect. This strengthens the overall buoyancy force, leading to a more intense primary circulation cell. The streamlines become densely packed, indicating higher fluid velocities. The isotherms reflect this by showing a significantly warmer core region. The thermal boundary layers may become thinner and more distorted as the internally heated fluid vigorously rises and interacts with the boundary-driven flow, enhancing thermal mixing.

When $Q = 0$, the system is devoid of internal heat generation. The flow and temperature fields are driven solely by the boundary conditions. The resulting streamline pattern shows a strong, classic buoyancy-driven vortex, and the isotherms depict heat transfer from the hot to the cold wall through a combination of advection and conduction, without internal thermal forcing.

For $Q < 0$, which corresponds to an internal heat sink, the phenomenon of thermal suppression becomes evident. The heat sink absorbs thermal energy from the fluid, counteracting the buoyancy effect generated by the hot wall. This leads to a marked weakening of the flow circulation, as seen in the sparser and less contorted streamlines. The isotherm patterns undergo a dramatic change: they become notably straighter and more parallel, resembling a conduction-like profile. This indicates that the internal heat absorption is effectively damping the convective strength, pulling the system back towards a less efficient, diffusion-dominated heat transfer regime despite the high external Ra. The core temperature of the fluid also decreases substantially compared to the $Q \geq 0$ cases.

Fig. (**6**) demonstrates the role of internal heat generation/absorption in the double undulation configuration. The complex geometry leads to a more nuanced response to changes in Q compared to the single cavity case. At this high $Ra = 10^6$, the base flow is multi-cellular, but the strength and structure of these cells are profoundly influenced by internal heating effects.

For $Q > 0$ (internal heat generation), the already vigorous multi-cellular flow is significantly intensified. The additional buoyancy from volumetric heating strengthens all existing vortices, leading to higher fluid velocities, as

evidenced by the densely packed streamlines in both undulations. The isotherms show a markedly warmer core and highly distorted thermal plumes. The heat source promotes stronger thermal mixing throughout the domain and enhances the interaction between the adjacent circulation cells, potentially leading to more complex, smaller-scale flow structures within the cavities.

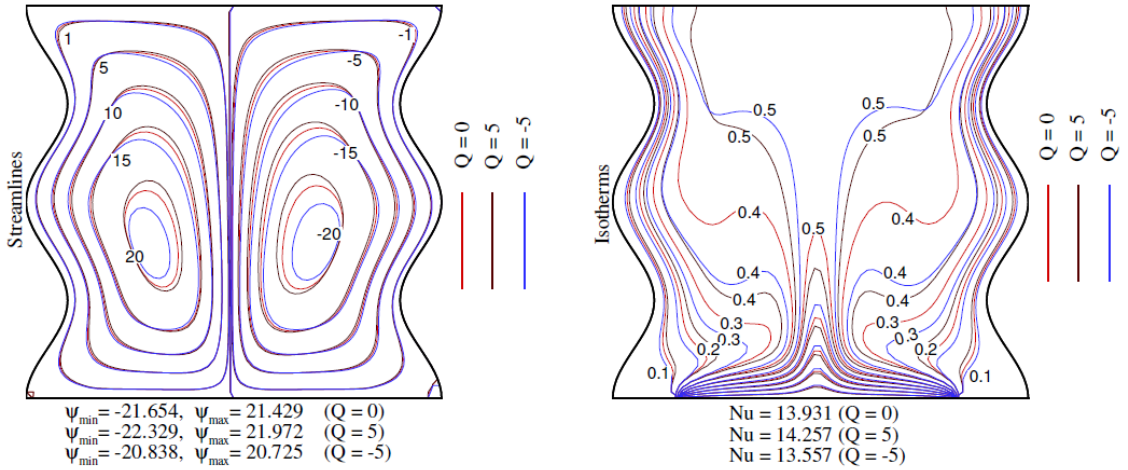

Figure 6: Streamlines (left) and isotherm contours (right) for the double-undulation wall configuration showing the influence of the heat generation/absorption parameter Q ($Q = 0{,}5, -5$) on convective flow patterns and temperature distribution at $Ha = 30$, $Ra = 10^6$, $\delta_0 = 1$, $\gamma = \pi/2$, and $\varphi_{hnp} = 2\%$. The double undulation alters vortex structure and enhances thermal mixing compared with the single-undulation case, with higher Q producing stronger convection.

In the absence of internal heat generation ($Q = 0$), the flow is governed solely by buoyancy forces arising from the imposed boundary temperature gradients and by the geometric modulation of the cavity walls. At $Ra = 10^6$, these combined effects lead to the formation of a segmented multi-vortex structure, which represents the natural convective equilibrium state for the present wavy configuration. The isotherms exhibit pronounced undulations that closely follow the local flow circulation within each geometric wave, reflecting the strong coupling between wall-curvature-induced flow separation and convective heat transport.

For $Q < 0$ (internal heat absorption), a dramatic suppression of the convective activity is observed. The heat sink absorbs energy, dampening the local buoyancy forces that drive each vortex. This causes a severe weakening of the flow, visible in the sparse, wide-spaced streamlines. The distinct, strong vortices observed at $Q \geq 0$ degrade into feeble, poorly defined circulation zones. The corresponding isotherms undergo a striking transformation, becoming straighter and significantly less contorted. This indicates a regression from a complex, convection-dominated regime towards a conduction-like state, where the intricate thermal patterns are "smoothed out" by the loss of thermal energy and the consequent decay of fluid motion. The heat sink effectively nullifies the flow complexity that the double undulation geometry is designed to promote.

4.1.3. Effect of Magnetic Orientation for Different Configuration of the Considered Domain

The influence of the magnetic field strength, governed by the Hartmann number (Ha), on suppressing convective flow is depicted in Fig. (**7**) (single undulation) and Fig. (**8**) (double undulation). The results are presented for increasing Ha, with other parameters held constant at $Ra = 10^6$, $Q = 2$, $\delta_0 = 1$, $\varphi_{\mathrm{hnp}} = 0.02$, and $\gamma = \pi/2$.

Fig. (**7**) demonstrates the damping effect of the magnetic field in the single undulation configuration. At low Ha, a strong, asymmetric primary vortex characterizes the flow, and the isotherms are highly distorted, indicating vigorous convection. As Ha increases, the Lorentz force opposes the buoyancy-driven flow, leading to a significant weakening of the vortex. The streamlines become sparser, and the flow cell shrinks and centralizes. Consequently, the isotherms transition from curved, convective patterns to straighter, more parallel lines, signifying a regression towards a conduction-dominated heat transfer regime as the magnetic suppression overwhelms the buoyant forces at $Ra = 10^6$.

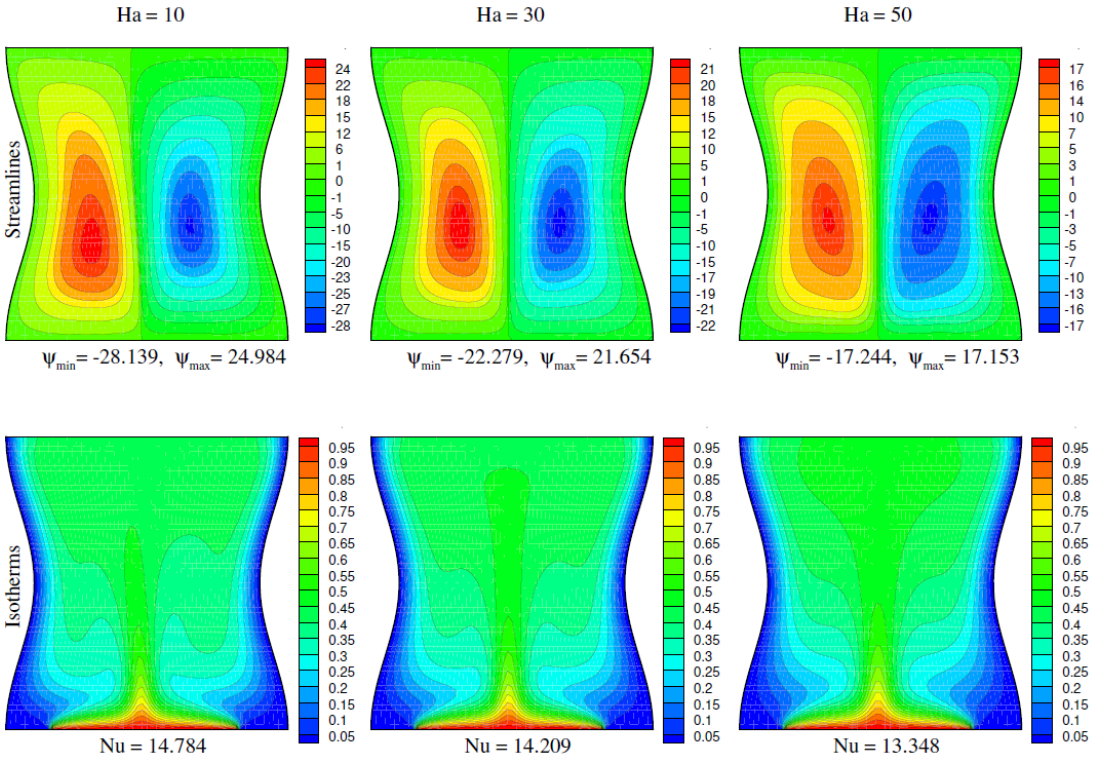

Figure 7: Streamlines (top row) and isotherm contours (bottom row) for the single-undulation wall configuration showing the effect of the Hartmann number Ha ($Ha = 10,30,50$) on flow structure and temperature distribution at $Ra = 10^6$, $Q = 2$, $\delta_0 = 1$, $\gamma = \pi/2$, and $\varphi_{hnp} = 2\%$. Increasing Ha suppresses fluid motion due to enhanced magnetic damping, weakens vortex intensity, and reduces convective heat transfer.

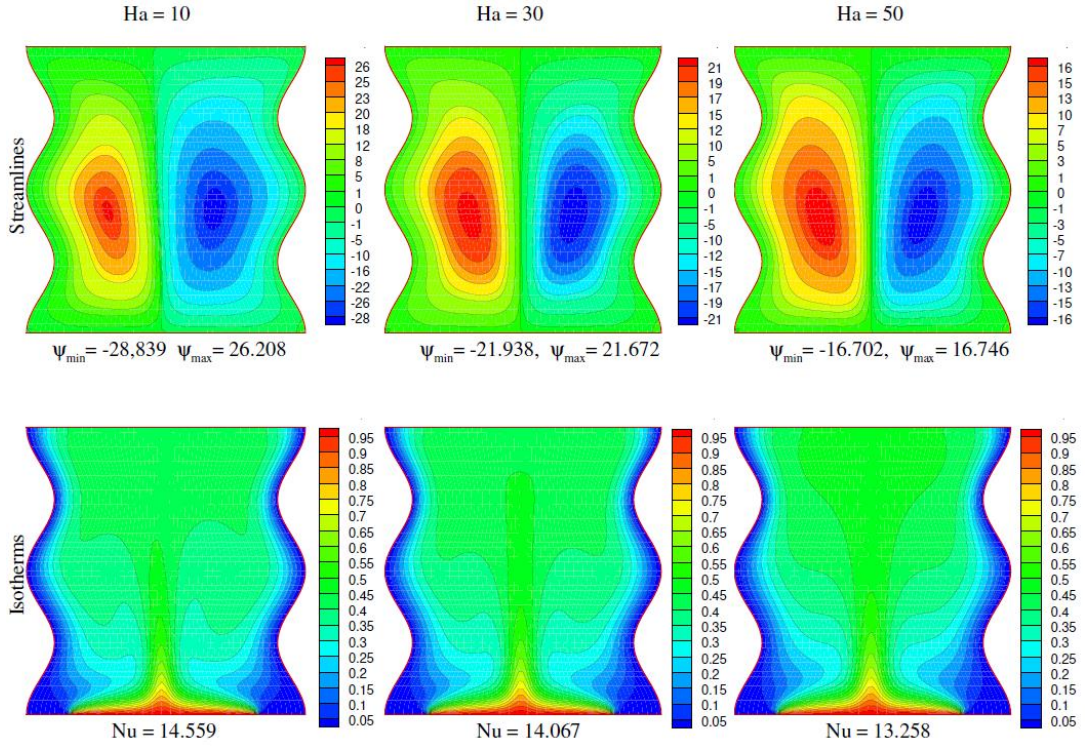

Figure 8: Streamlines (top row) and isotherm contours (bottom row) for the double-undulation wall configuration illustrating the influence of the Hartmann number Ha ($Ha = 10,30,50$) on convective flow patterns and thermal fields at $Ra = 10^6$, $Q = 2$, $\delta_0 = 1$, $\gamma = \pi/2$, and $\varphi_{hnp} = 2\%$. Stronger magnetic fields attenuate circulation strength and modify vortex topology, leading to diminished heat transfer rates.

Fig. (**8**) reveals the magnetic damping effect on the more complex double undulation geometry at a higher $Ra = 10^6$. At low Ha, the flow is multi-cellular, with distinct vortices occupying each cavity, and the isotherms are highly complex and wavy. With increasing Ha, the Lorentz force progressively dampens these vortices. The smaller, secondary vortices are the first to be suppressed and vanish, followed by the weakening and simplification of the primary circulation cells. The corresponding isotherms gradually lose their waviness and become smoother and more linear. This shows that a strong magnetic field can effectively erase the geometric complexity of the flow, homogenizing the temperature field and stifling the local heat transfer enhancement generated by the undulations.

Thus, increasing the Hartmann number consistently suppresses fluid motion and convective heat transfer in both configurations. However, the double undulation's complex, multi-cellular flow is more susceptible to magnetic damping, as the geometry-induced secondary vortices are stabilized by inertia at high Ra but are readily eliminated by the application of a strong magnetic field.

4.2. Evaluation of Thermal Performance and Volumetric Flow Rate through Nusselt Number and Streamfunction (ψ)

The thermal performance and volumetric flow rate are key metrics for evaluating the efficiency of any thermal system. In convective heat transfer studies, these are quantified by the average Nusselt number (Nu_{av}) and the maximum streamfunction ($\psi_{\max}$), respectively. An increasing trend in the Nusselt number indicates strong thermal mixing within the flow domain, which ensures better thermal efficiency. Conversely, a downtrend in the Nusselt number signifies poor thermal performance. On the other hand, higher values of $\psi_{\max}$ correspond to a greater volumetric flow rate (per unit depth), reflecting stronger circulation intensity within the enclosure.

Fig. (**9**) presents the combined effects of the internal heat parameter (Q) and the enclosure configuration on these critical performance metrics, with other parameters fixed at $Ra = 10^6$, $Ha = 30$, $\delta_0 = 1$, $\gamma = \pi/2$, and $\varphi_{\mathrm{hnp}} = 2\%$.

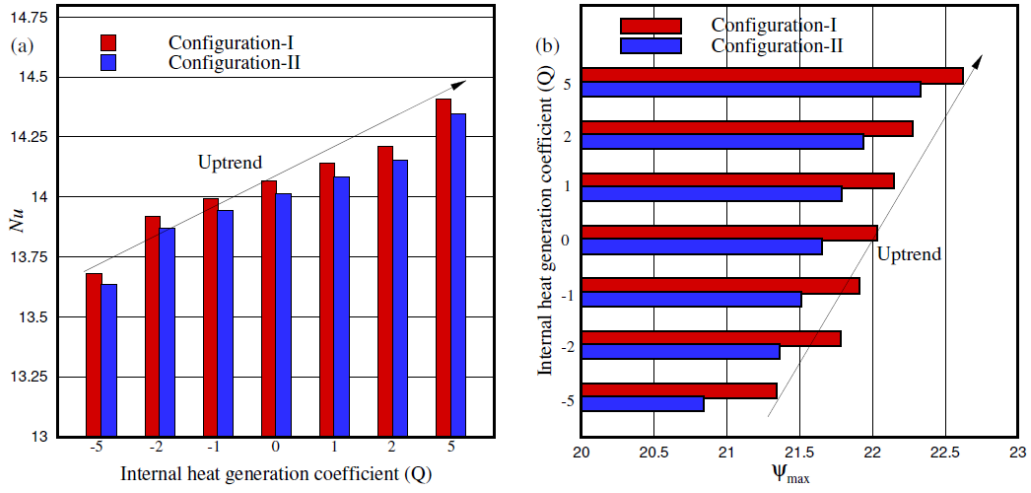

Figure 9: (**a**) Nu_{av} (**b**) $\psi_{\max}$ for different values of Q at $Ra = 10^6$, $Ha = 30$, $\delta_0 = 1$, $\gamma = \frac{\pi}{2}$ and $\varphi_{hnp} = 2\%$ in different configurations.

Subfigure (**9a**), depicting the average Nusselt number (Nu_{av}), reveals a clear trend: Nu_{av} increases with Q for both configurations. This is physically consistent, as a positive Q (internal heat generation) augments the buoyancy force, intensifying fluid motion and convective mixing, thereby enhancing heat transfer from the walls. The double undulation configuration consistently exhibits a higher Nu_{av} than the single undulation across all Q values. This performance superiority is attributed to the more complex flow path and the multi-cellular flow structure in the double undulation, which promotes greater fluid mixing and disrupts thermal boundary layers more effectively than the simpler, single-vortex flow in the single undulation.

Subfigure (**9b**), showing the maximum streamfunction ($\psi_{\max}$), demonstrates that the flow strength also increases with Q for both geometries, following the same buoyancy-enhancement mechanism. The double undulation configuration consistently registers a higher $\psi_{\max}$ than its single undulation counterpart. This indicates that the geometric complexity of the double undulation not only creates a more complex flow structure but also facilitates a stronger overall circulation within the domain. The stronger flow directly contributes to the enhanced thermal mixing observed in subfigure (**9a**).

5. Conclusion

This study presents a numerical analysis of magneto-thermo-convective heat transfer of an Ag–MgO/water hybrid nanofluid in a wavy-walled cavity with localized bottom heating, incorporating magnetic-field-dependent viscosity (MFDV) effects. The combined influence of cavity undulation, magnetic field orientation, and variable viscosity under magnetic intensity has not been previously reported for this configuration. The findings provide useful guidelines for designing thermally efficient enclosures subjected to magnetic control.

The main outcomes of the present work are summarized as follows:

1. The double-undulation cavity (Configuration-II) produces stronger circulation and better fluid mixing than the single-undulation cavity. This leads to higher average Nusselt number and larger streamfunction magnitude. Geometric modification is therefore an effective passive technique for heat transfer enhancement.
2. Increasing the Hartmann number suppresses fluid motion due to the Lorentz force. As a result, convection weakens and heat transfer decreases.
3. The magnetic-field-dependent viscosity parameter further alters the flow by increasing local resistance to motion. This introduces an additional level of magnetic control over thermal performance.
4. Higher Rayleigh numbers significantly strengthen buoyancy-driven circulation and enhance heat transfer.
5. Internal heat generation intensifies vortices and increases thermal gradients, whereas internal heat absorption weakens convection and shifts the system toward conduction-dominated transport.
6. The orientation of the magnetic field modifies vortex structure and affects the degree of flow suppression.
7. Maximum thermal performance is achieved for high Ra, double-undulation geometry, and positive heat generation, while strong magnetic fields and heat absorption reduce system efficiency.

From a practical viewpoint, the present results indicate that combining geometric tailoring with magnetic-field regulation and controlled internal heating can be used to optimize heat transfer in electronic cooling devices, energy storage systems, and thermal management enclosures.

Nomenclature

B_0	Magnetic effect (Amp.m-1)
C_p	Specific heat (J.kg-1.K-1)
g	Gravitational acceleration (ms-2)
Ha	Hartmann number ($B_0 L\sqrt{\sigma_{nf}/\rho_{nf}\nu_f}$)
k	Thermal conductivity (W.m-1.K-1)
d_p	Radius of nanoparticles, nm
p	Dimensional pressure (N.m-2)

P	Dimensionless pressure
Pr	Prandtl number
Ra	Rayleigh number
Q_0	Dimensional of heat generation or absorption
Q	Dimensionless of heat generation or absorption
Nu	Nusselt number
U, V	Dimensionless velocities in non-dimensional X, Y directions respectively

Greek Letters

ξ,η	Dimensionless coordinate in computational plane
ν	Kinematic viscosity (m2.s-1)
ρ	Density (kg.m-3)
μ	Dynamic viscosity (Pa.s)
γ	Inclination angle
α	Thermal diffusivity (m2.s-1)
β	Thermal expansion coefficient (K-1)
σ	Electrical conductivity (μS.cm-1)
φ	Solid volume fraction
δ_0	Viscosity parameter
T_h	Temperature of heat sources (K)
T_c	Temperature of heat sinks (K)
T	Dimensional temperature
θ	Dimensionless temperature

Subscripts

i, j	cell faces
f	fluid
hnp	hybrid nano particle
hnf	hybrid nanofluid
av	average
c	cold wall
h	hot wall

Conflict of Interest

The authors declare that they have no known competing financial interests or personal relationships that could have appeared to influence the work reported in this paper.

Funding

This research received no external funding.

References

[1] Sarkar UK, Biswas N, Oztop HF. Multiplicity of solution for natural convective heat transfer and entropy generation in a semi-elliptical enclosure. Phys Fluids. 2021; 33: 013601. https://doi.org/10.1063/5.0037260

[2] Wen X, Wang LP, Guo Z. Designing a consistent implementation of the discrete unified gas-kinetic scheme for the simulation of three-dimensional compressible natural convection. Phys Fluids. 2021; 33: 046101. https://doi.org/10.1063/5.0045227

[3] Mohammadfam Y, Heris SZ. Experimental study of the influence of Fe_2O_3, MWCNT–Fe_2O_3 and Fe_2O_3@MWCNT nanoparticles on thermophysical characteristics and laminar convective heat transfer of nanofluids. Surf Interfaces. 2023; 43: 103506. https://doi.org/10.1016/j.surfin.2023.103506

[4] Samadzadeh A, Heris SZ, Hashim I, Mahian O. Experimental investigation on natural convection of non-covalently functionalized MWCNT nanofluids: effects of aspect ratio and inclination angle. Int Commun Heat Mass Transf. 2020; 111: 104473. https://doi.org/10.1016/j.icheatmasstransfer.2019.104473

[5] Heris SZ, Zolfagharian N, Mousavi SB, Nami SH. Enhancing the synergistic properties of plate heat exchangers using nanohybrid MWCNT–SiO_2 EG-based nanofluids. J Therm Anal Calorim. 2025; 150: 6225-34. https://doi.org/10.1007/s10973-025-14165-0

[6] Heris SZ, Pasvei S, Pourpasha H, Mohammadfam Y, Sharifpur M, Meyer J, *et al*. Experimental analysis of graphene-COOH/water and TiO_2/water nanofluids in plate heat exchangers. Renew Energy. 2025; 245: 122822. https://doi.org/10.1016/j.renene.2025.122822

[7] Arjun KS, Rakesh K. Heat transfer in magnetohydrodynamic nanofluid flow past a circular cylinder. Phys Fluids. 2020; 32: 045112. https://doi.org/10.1063/5.0005095

[8] Avramenko AA, Shevchuk IV, Abdallah S, Blinov DG, Tyrinov AI. Self-similar analysis of fluid flow, heat, and mass transfer at orthogonal nanofluid impingement onto a flat surface. Phys Fluids. 2017; 29: 052005. https://doi.org/10.1063/1.4983061

[9] Khan D, Asogwa KK, Alqahtani T, Algarni S, Alqahtani S, Akbar MA. Two-phase free convection flow of dusty Jeffrey fluid between vertical parallel plates. J Math. 2022; 2022: 8470139. https://doi.org/10.1155/2022/8470139

[10] Khan D, Kumam P, ur Rahman A, Ali G, Sitthithakerngkiet K, Watthayu W, *et al*. Newtonian heating effects on Couette flow of viscoelastic dusty fluid in a rotating frame. Heliyon. 2022; 8(9): e10538. https://doi.org/10.1016/j.heliyon.2022.e10538

[11] Mahariq I, Ghazwani HA, Shah MA. Enhancing heat and mass transfer in MHD tetra-hybrid nanofluid on solar collector plate. Results Eng. 2024; 103163. https://doi.org/10.1016/j.rineng.2024.103163

[12] Biswas N, Mahapatra PS, Manna NK. Buoyancy-driven fluid and energy flow in protruded heater enclosure. Meccanica. 2016; 51: 2159-84. https://doi.org/10.1007/s11012-016-0366-6

[13] Manna NK, Mandal DK, Bhattacharjee K, Dikshit N, Biswas N, Chamkha AJ. Thermal management of magneto-ferrofluid operated circular systems. Phys Fluids. 2025; 37: 103616. https://doi.org/10.1063/5.0285122

[14] Choi SUS. Enhancing thermal conductivity of fluids with nanoparticles. ASME Fluids Eng Div. 1995; 231: 99-105. https://doi.org/10.1115/IMECE1995-0926

[15] Chattopadhyay A, Pandit SK, Oztop HF. Thermal performance and entropy generation in a wavy enclosure with moving walls. Eur J Mech B Fluids. 2020; 79: 12-26. https://doi.org/10.1016/j.euromechflu.2019.08.006

[16] Cho CC. Natural convection of Cu-water nanofluid in an enclosed cavity with porous effect. Phys Fluids. 2020; 32: 103607. https://doi.org/10.1063/5.0024773

[17] Izadi M, Behzadmehr A, Shahmardan MM. Effects of inclination angle on laminar mixed convection of a nanofluid in an annulus. Chem Eng Commun. 2015; 202(12): 1693-702. https://doi.org/10.1080/00986445.2014.910770

[18] Verma SK, Tiwari AK. Progress of nanofluid application in solar collectors. Energy Convers. Manag. 2015; 100: 324-46. https://doi.org/10.1016/j.enconman.2015.04.071

[19] Xiong Q, Hajjar A, Alshuraiaan B, Izadi M, Altnji S, Shehzad SA. State-of-the-art review of nanofluids in solar collectors. J Clean Prod. 2021; 127528. https://doi.org/10.1016/j.jclepro.2021.127528

[20] Bahiraei B, Heshmatian S. Electronics cooling with nanofluids. Energy Convers Manag. 2018; 172: 438-56. https://doi.org/10.1016/j.enconman.2018.07.047

[21] Soylu SK, Atmaca M, Asilturk M, Dogan A. Improving heat transfer performance of an automobile radiator using Cu- and Ag-doped TiO_2-based nanofluids. Appl Therm Eng. 2019; 157: 113743.

[22] Haddad Z, Abid C, Oztop HF, Mataoui A. A review on how researchers prepare their nanofluids. Int J Therm Sci. 2014; 76: 168-89. https://doi.org/10.1016/j.ijthermalsci.2013.08.010

[23] Delouei AA, Sajjadi H, Izadi M, Mohebbi R. Simultaneous effects of nanoparticles and ultrasonic vibration on inlet turbulent flow: an experimental study. Appl Therm Eng. 2019; 146: 268-77. https://doi.org/10.1016/j.applthermaleng.2018.09.113

[24] Ma Y, Yang Z. Simplified and highly stable thermal lattice Boltzmann method simulation of hybrid nanofluid convection at high Rayleigh numbers. Phys Fluids. 2020; 32: 012009. https://doi.org/10.1063/1.5139092

[25] Al-Srayyih BM, Gao S, Hussain SH. Natural convection flow of a hybrid nanofluid in a square enclosure partially filled with a porous medium. Phys Fluids. 2019; 31: 043609. https://doi.org/10.1063/1.5080671

[26] Sarkar J, Ghosh P, Adil A. A review on hybrid nanofluids: recent research, development and applications. Renew. Sustain. Energy Rev. 2015; 43: 164-77. https://doi.org/10.1016/j.rser.2014.11.023

[27] Tyagi PK, Kumar R, Mondal PK. State-of-the-art nanofluid spray and jet impingement cooling. Phys Fluids. 2020; 32: 121301. https://doi.org/10.1063/5.0033503

[28] Mohebbi R, Izadi M, Chamkha AJ. Heat source location and natural convection in a C-shaped enclosure saturated by a nanofluid. Phys Fluids. 2017; 29: 122009. https://doi.org/10.1063/1.4993866

[29] Chamkha AJ, Rashad A, Mansour MA, Armaghani T, Ghalambaz M. Effects of heat sink and source and entropy generation on MHD mixed convection of a Cu-water nanofluid. Phys Fluids. 2017; 29: 052001. https://doi.org/10.1063/1.4981911

[30] Manna NK, Mondal C, Biswas N, Sarkar UK, Oztop HF, Abu-Hamdeh NH. Effect of multibanded magnetic field on convective heat transport in porous systems filled with hybrid nanofluid. Phys Fluids. 2021; 33: 053604. https://doi.org/10.1063/5.0043461

[31] Yan SR, Izadi M, Sheremet MA, Pop I, Oztop HF, Afrand M. Inclined Lorentz force impact on convective-radiative heat exchange of micropolar nanofluid. Int Commun Heat Mass Transf. 2020; 117: 104762. https://doi.org/10.1016/j.icheatmasstransfer.2020.104762

[32] Sheikholeslami M, Vajravelu K. Nanofluid flow and heat transfer in a cavity with variable magnetic field. Appl Math Comput. 2017; 298: 272-82. https://doi.org/10.1016/j.amc.2016.11.025

[33] Dogonchi AS, Waqas M, Seyyedi SMS, Hashemi-Tilehnoee M, Ganji DD. Modified Fourier approach for nanofluid heat generation in a semi-circular enclosure. Int Commun Heat Mass Transf. 2020; 111: 104430. https://doi.org/10.1016/j.icheatmasstransfer.2019.104430

[34] Roy NC. Magnetohydrodynamic natural convection flow of a nanofluid due to sinusoidal surface temperature variations. Phys Fluids. 2020; 32: 022003. https://doi.org/10.1063/1.5143516

[35] Mehryan SAM, Izadi M, Namazian Z, Chamkha AJ. Natural convection of MWCNT–Fe_2O_3/water magnetic hybrid nanofluid in porous media. J Therm Anal Calorim. 2019; 138: 1541-55. https://doi.org/10.1007/s10973-019-08164-1

[36] Pandit SK, Goswami KD, Chattopadhyay A, Oztop HF. Magnetohydrodynamics and magnetic field-dependent viscosity effects on thermogravitational convection. Phys Fluids. 2021; 33: 010701. https://doi.org/10.1063/5.0061451

[37] Mahian O, Kolsi L, Amani M, Estell P, Ahmadi G, Kleinstreuer C, *et al*. Recent advances in modeling and simulation of nanofluid flows—Part I. Phys Rep. 2019; 790: 1-48. https://doi.org/10.1016/j.physrep.2018.11.004

[38] Hussain S, Ahmed SEA, Akbar T. Entropy generation analysis in MHD mixed convection of hybrid nanofluid in an open cavity. Int J Heat Mass Transf. 2017; 114: 1054-66. https://doi.org/10.1016/j.ijheatmasstransfer.2017.06.135

[39] Esfe MH, Arani AAA, Rezaie M, Yan WM, Karimipour A. Experimental determination of thermal conductivity and viscosity of Ag–MgO/water hybrid nanofluid. Int Commun Heat Mass Transf. 2015; 66: 189-95. https://doi.org/10.1016/j.icheatmasstransfer.2015.06.003

[40] Chattopadhyay A, Goswami KD, Pandit SK, Sheremet MA. Thermal performance in transient MHD thermogravitational convection of nanofluid. J Therm Anal Calorim. 2021; 146: 1255-81. https://doi.org/10.1007/s10973-020-10077-3

[41] Goswami KD, Chattopadhyay A, Pandit SK, Sheremet MA. Brownian motion of magnetonanofluid flow in an undulated partially heated enclosure. Int J Mech Sci. 2021; 198: 106346. https://doi.org/10.1016/j.ijmecsci.2021.106346

[42] Van der Vorst HA. BiCGSTAB: a fast and smoothly converging variant of BiCG for nonsymmetric linear systems. SIAM J Sci Comput. 1992; 13(2): 631-44. https://doi.org/10.1137/0913035

[43] Ho CJ, Liu WK, Chang YS, Lin CC. Natural convection heat transfer of alumina-water nanofluid in vertical square enclosures. Int J Therm Sci. 2010; 49: 1345-53. https://doi.org/10.1016/j.ijthermalsci.2010.02.013

[44] Saghir MZ, Ahadi A, Mohamad A, Srinivasan S. Water–aluminum oxide nanofluid benchmark model. Int J Therm Sci. 2016; 109: 148-58. https://doi.org/10.1016/j.ijthermalsci.2016.06.002

[45] Al-Amiri A, Khanafer K, Bull J, Pop I. Effect of sinusoidal wavy bottom surface on mixed convection in a lid-driven cavity. Int J Heat Mass Transf. 2007; 50: 1771-80. https://doi.org/10.1016/j.ijheatmasstransfer.2006.10.008

[46] Hayat T, Qayyum S, Imtiaz M, Alsaedi A. Comparative study of silver and copper water nanofluids with mixed convection. Int J Heat Mass Transf. 2016; 102: 723-32. https://doi.org/10.1016/j.ijheatmasstransfer.2016.06.059

[47] Ma Y, Mohebbi R, Rashidi MM, Yang Z. MHD convective heat transfer of Ag–MgO/water hybrid nanofluid in a channel. Int J Heat Mass Transf. 2019; 137: 714-26. https://doi.org/10.1016/j.ijheatmasstransfer.2019.03.169